PNAS RESEARCH ARTICLE | EARTH, ATMOSPHERIC, AND PLANETARY SCIENCES

Anthropogenic short-lived halogens increase human exposure to mercury contamination due to enhanced mercury oxidation over continents

Xiao Fu[a,1,2], Xianyi Sun[a,1], Oleg Travnikov[b,1], Qinyi Li[c,d,e,1], Chuang Qin[a], Carlos A. Cuevas[c], Rafael P. Fernandez[f], Anoop S. Mahajan[g], Shuxiao Wang[h], Tao Wang[d], and Alfonso Saiz-Lopez[c,2]

Edited by Joel Blum, University of Michigan; received August 31, 2023; accepted February 6, 2024

Mercury (Hg) is a contaminant of global concern, and an accurate understanding of its atmospheric fate is needed to assess its risks to humans and ecosystem health. Atmospheric oxidation of Hg is key to the deposition of this toxic metal to the Earth's surface. Short-lived halogens (SLHs) can provide halogen radicals to directly oxidize Hg and perturb the budget of other Hg oxidants (e.g., OH and O_3). In addition to known ocean emissions of halogens, recent observational evidence has revealed abundant anthropogenic emissions of SLHs over continental areas. However, the impacts of anthropogenic SLHs emissions on the atmospheric fate of Hg and human exposure to Hg contamination remain unknown. Here, we show that the inclusion of anthropogenic SLHs substantially increased local Hg oxidation and, consequently, deposition in/near Hg continental source regions by up to 20%, thereby decreasing Hg export from source regions to clean environments. Our modeling results indicated that the inclusion of anthropogenic SLHs can lead to higher Hg exposure in/near Hg source regions than estimated in previous assessments, e.g., with increases of 8.7% and 7.5% in China and India, respectively, consequently leading to higher Hg-related human health risks. These results highlight the urgent need for policymakers to reduce local Hg and SLHs emissions. We conclude that the substantial impacts of anthropogenic SLHs emissions should be included in model assessments of the Hg budget and associated health risks at local and global scales.

short-lived halogens | mercury oxidation | mercury exposure | anthropogenic emissions

Atmospheric mercury (Hg) is a pollutant of global concern (1, 2). The methylation and bioaccumulation of Hg deposited in ecosystems can produce methylmercury (MeHg), which is related to neurocognitive deficits in fetuses and cardiovascular damage in adults (3, 4). Hg is emitted mainly in elemental form (Hg^0) with a long lifetime (several months to a year) (5, 6), which allows global transport and deposition to distant pristine environments, including polar and open ocean regions. Oxidized Hg ($Hg^{I,II}$) has a much shorter lifetime (several hours to days), leading to Hg deposition locally or regionally (7, 8). Therefore, the chemical conversion of Hg^0 to $Hg^{I,II}$ significantly affects the scale and spatial pattern of global Hg deposition, and consequently its health-related effects.

Short-lived halogens (SLHs; chlorine-, bromine-, and iodine-containing species with a lifetime <6 mo) have considerable impacts on the oxidation of elemental Hg. The photochemical breakdown of SLHs releases halogen atoms, especially bromine (Br) atoms, which are known to be major Hg oxidants (9–12). Reactive halogen chemistry also affects the budget of other Hg oxidants, such as hydroxyl (OH) and hydroperoxyl (HO_2) radicals, ozone (O_3), and nitrogen dioxide (NO_2) (13–15). Previous studies have primarily focused on the significance of natural SLHs emissions (16–19), such as inorganic chlorine (Cl) and Br from dechlorination/debromination of sea salt, halocarbons from marine organisms, and inorganic iodine (I) from the oxidation of seawater iodide by deposited O_3. Rapid Hg oxidation is frequently observed in the regions with abundant natural halogens (11, 20–22), such as polar regions, salt lakes, and the marine atmosphere. Modeling studies have also revealed the importance of natural SLHs emissions on global Hg cycling (8, 23, 24).

Over the last decade, observational evidence has demonstrated the emission of anthropogenic SLHs and active halogen chemistry over continental areas (25–28), especially in polluted regions with intensive anthropogenic activities (e.g., China and India), significantly influencing atmospheric oxidation capacity and air pollution (29–31). The high concentrations of BrCl observed in northern China and Br_2 in southern China could increase the local conversion rates of Hg^0 to $Hg^{I,II}$ by approximately 35- and 10-fold, respectively (27, 28). Concomitantly, high Hg emissions and high-density populations exist over these continental areas (5, 6). However, despite this observational evidence, the impacts of anthropogenic SLHs emissions and chemistry on Hg cycling at regional and

Significance

Atmospheric oxidation of mercury (Hg), a global contaminant, is key to its transport and deposition to the surface. Short-lived halogens (SLHs) play an important role in global Hg oxidation. Recent observational evidence has demonstrated the presence of anthropogenic SLHs over continental areas, which are neglected in previous Hg modeling assessments. Our results suggest that the role of colocated anthropogenic SLHs emissions with Hg in controlling the local Hg^0-$Hg^{I,II}$ conversion, and consequently in regulating Hg deposition, potentially increases human mercury exposure, especially in the vicinity of SLHs and Hg source regions. We conclude that the substantial impacts of anthropogenic SLHs emissions should be included in mercury assessments to improve our knowledge of Hg budget and its associated health risks.

The authors declare no competing interest.

This article is a PNAS Direct Submission.

[1]X.F., X.S., O.T. and Q.L. contributed equally to this work.

[2]To whom correspondence may be addressed. Email: fu.xiao@sz.tsinghua.edu.cn or a.saiz@csic.es.

This article contains supporting information online at https://www.pnas.org/lookup/suppl/doi:10.1073/pnas.2315058121/-/DCSupplemental.

Published March 11, 2024.

global scales and the resulting health effects have not yet been explored.

In this study, we conducted emission-driven simulations to quantify the global impacts of anthropogenic SLHs emissions on Hg speciation and deposition, using CAM-Chem (Community Atmosphere Model with Chemistry) with a state-of-the-art scheme of natural and anthropogenic SLHs emissions and chemistry, and GLEMOS (Global European Monitoring and Evaluation Program Multimedia Modeling System) with state-of-the-art Hg chemistry (see *CAM-Chem Simulation* and *GLEMOS Simulation* in *Materials and Methods*). We further assessed their impacts on Hg-related health risks based on epidemiology-based dose–response relationships. Our modeling results suggest that the inclusion of anthropogenic SLHs in global models, through their efficient oxidation of modeled Hg, can substantially increase the modeled Hg deposition over land and coastal oceans, potentially resulting in greater human exposure to Hg contamination than previously identified, especially in countries with large Hg emissions.

Results

Anthropogenic Halogen Effects on Hg^0-$Hg^{I,II}$ Conversion. We conducted two main simulations, including the NoCont and HAL cases. In the NoCont case, we considered only natural SLHs emissions, mainly from biogenic and photochemical processes in the ocean and polar regions. In the HAL case, we considered both natural sources plus anthropogenic SLHs emissions (see *Emission of Anthropogenic Inorganic Halogens* in *Materials and Methods*). The difference between the HAL and NoCont cases was considered to be the effect of anthropogenic SLHs emissions.

Anthropogenic SLHs emissions showed a similar spatial pattern to anthropogenic Hg emissions (*SI Appendix*, Fig. S1). As large Hg emitters, China and India collectively contributed 20%, 53%, and 60% of global anthropogenic chlorine, bromine, and iodine emissions, respectively. Such colocated emissions of anthropogenic SLHs with Hg resulted in a considerable increase in oxidized Hg over its source region and the surrounding area (Fig. 1*d*). Our modeling results showed that the simulated surface $Hg^{I,II}$ concentrations in the HAL case were 30% to 40% larger than in the NoCont case, over some areas in China and India, and their surrounding regions such as East China Sea, Yellow Sea, Sea of Japan, Japan, Korean Peninsula, and the Bay of Bengal. This resulted in better agreement of simulated Hg wet deposition, which mostly consists of $Hg^{I,II}$, with observations at urban sites, reducing the overall underestimation from 5.9% to 3.0% and slightly increasing spatial correlation (see more details about model validation in *SI Appendix*). Compared with the NoCont case, the simulated Hg^0

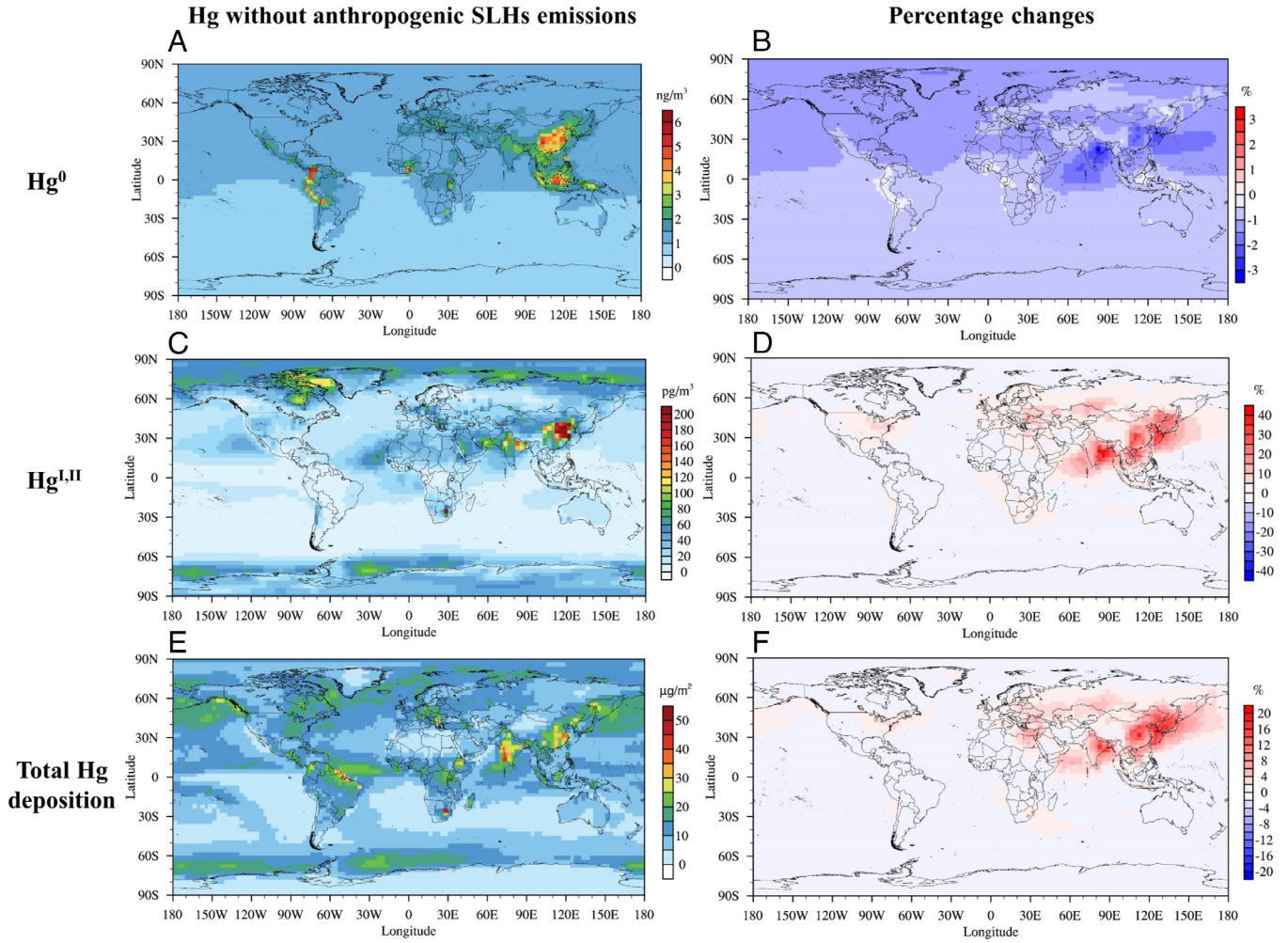

Fig. 1. Spatial patterns of anthropogenic SLHs-driven changes in Hg speciation and deposition. Surface Hg^0 (ng/m^3), $Hg^{I,II}$ (pg/m^3), and total Hg deposition ($\mu g/m^2$) without anthropogenic SLHs emissions (NoCont) are shown on the *Left* (*A*, *C*, and *E*). Their percentage changes (%) driven by anthropogenic SLHs emissions relative to the NoCont case are shown on the *Right* (*B*, *D*, and *F*). High Hg concentrations and depositions occurred in regions with high anthropogenic Hg emissions (see *SI Appendix*, Fig. S1 for the emission distribution). Colocated anthropogenic SLHs emissions with Hg significantly increased $Hg^{I,II}$ and total Hg deposition in regions with high Hg emissions and severe Hg pollution.

in the HAL case exhibited global decreases (up to −3%), with less marked heterogeneity than that of $Hg^{I,II}$, due to its longer lifetime (Fig. 1*B*). This decrease led to the simulated average Hg^0 concentration in the HAL case (1.69 ng m^{-3}) being closer to the observations (1.63 ng m^{-3}) than in the NoCont case (1.71 ng m^{-3}).

Such impact on the Hg^0-$Hg^{I,II}$ conversion resulted from the changes in Hg oxidation chemistry caused by anthropogenic SLHs emissions through direct and indirect pathways. On one hand, the inclusion of anthropogenic SLHs emissions directly supplied more halogen radicals (Br and Cl) to oxidize Hg^0. The conversion and photolysis of SLHs increased the surface concentrations of Br and Cl atoms in continental regions (*SI Appendix*, Fig. S2), with the largest increases (exceeding 800% in the HAL case relative to the NoCont case) occurring in localized regions with large anthropogenic SLHs emissions due to their short lifetime. In the HAL case, we determined that the dominant $Hg^{I,II}$ species in the troposphere were gaseous $HgCl_2$ (47%), gaseous HgBrOH (9%) and total particulate Hg (43%). This $Hg^{I,II}$ partitioning was similar to previous estimates by Shah et al. (12) despite slightly different assumptions about $Hg^{I,II}$ gas–particle interactions used in the model formulations (see more details in S1.2 in *SI Appendix*). In the surface air, close to anthropogenic SLHs emissions, the $Hg^{I,II}$ species with the largest increase in the HAL case compared with the NoCont case was HgBrOH (sum of gas and particulate) (*SI Appendix*, Fig. S3), whose changing spatial pattern was consistent with that of Br radical (*SI Appendix*, Fig. S4), implying the key role of Br radicals provided by anthropogenic SLHs emissions. $HgCl_2$ was the $Hg^{I,II}$ species with the second-high enhancement in the surface air, whose formation was driven by Cl radicals from anthropogenic SLHs emissions. On the other hand, anthropogenic SLHs emissions indirectly affected Hg^0-$Hg^{I,II}$ conversion through perturbing HO_X-NO_X-O_3 chemistry. Over continents, halogens enhanced the production of HO_X (OH and HO_2) and O_3 by initiating the oxidation of volatile organic compounds (VOCs), leading to the faster recycling of atmospheric radicals and O_3 production in the presence of NO_x (29, 30). Halogens (especially I and Br) can also reduce O_3 and HO_X directly by halogen reactions with O_3 and indirectly via transforming NO_2 into halogen nitrates. The combined effects of anthropogenic SLHs on Hg oxidants depended on the emitted species and the mixture of atmospheric compositions. Overall, compared with the NoCont case, the inclusion of anthropogenic SLHs emissions in the HAL case increased OH and HO_2, decreased NO_2 in most continental regions, and decreased O_3 except in polluted eastern China (*SI Appendix*, Fig. S5). The highest enhancement of surface OH, HO_2, and O_3 in polluted eastern China could reach 10%, 15%, and 5%, respectively. Overall, these halogen-driven nonlinear changes in Hg oxidants accelerated the chemical conversion of Hg^0 to $Hg^{I,II}$ in and near source regions.

Anthropogenic Halogen Effects on Hg Deposition. The changes in Hg^0-$Hg^{I,II}$ conversion driven by anthropogenic SLHs emissions significantly affected the magnitude and spatial pattern of global Hg deposition. The simulated average wet deposition of Hg in the HAL case (9.59 μg m^{-2} y^{-1}) was closer to the observations over available 134 measurement sites (9.64 μg m^{-2} y^{-1}) than that in NoCont case (9.46 μg m^{-2} y^{-1}). The correlation of simulated and observed values also slightly increased for the scenario with anthropogenic SLHs emissions (HAL) (see more details about model validation in *SI Appendix*). As shown in Fig. 1*E*, our modeling results showed that compared with the NoCont case, the inclusion of anthropogenic SLHs emissions in the HAL case considerably increased the total Hg deposition in the corresponding regions with large $Hg^{I,II}$ enhancements. The simulated total deposition increased by 7.7% and 6.4% in China and India, respectively, with larger enhancements of 10% to 20% localized over their polluted areas. Long-lived Hg is characterized by its long-range transport across different continents and oceans. Our modeling results showed that enhanced local Hg deposition driven by anthropogenic SLHs decreased the net Hg outflow from continental China and India by 10.8 and 4.6 Mg/y. It is noteworthy that anthropogenic SLHs simultaneously drove the Hg outflow to deposit more efficiently into the surrounding coastal ocean near Hg source regions, but leading to lower Hg transport to the remote areas. Compared with the NoCont case, the simulated total deposition in the HAL case increased by 14.5% and 8.9% in South Korea and Japan, respectively. Larger increases (up to 20%) in Hg deposition occurred in the East China Sea, Yellow Sea, and Bay of Bengal, while decreases were modeled in most open ocean regions. Over the continents far away from Hg and SLHs hotspots, such as Other America (America except the United States), Africa, and Oceania, the Hg deposition did not change much. Relocation of Hg deposition can affect Hg levels in the environment and food, leading to subsequent impacts on health risks.

Anthropogenic Halogen-Driven Increase in Hg Exposure and Human Health Effects. Next, we estimated the potential increase in MeHg exposure and Hg-related health risks associated with anthropogenic SLHs emissions (Fig. 2). Exposure from rice, freshwater fishes, and seafood was included in the analysis. Two health endpoints were selected as a consequence of food Hg exposure, including per-fetus intelligence quotient (IQ) decrements and death caused by cardiovascular effects (see *Changes in Hg Exposure and Health Effects* in *Materials and Methods*).

Compared with the assessment based on the NoCont case, the inclusion of anthropogenic SLHs emissions increased global MeHg exposure by 5% (Fig. 2*A*), with spatial heterogeneity associated with different food MeHg concentration changes and food intake structures in different regions. As large anthropogenic Hg and halogen emitter, the change of the per-capita MeHg exposure in China was estimated to be 8.7% (10.3 ng $kg^{-1}d^{-1}$). China's major producing areas of rice and freshwater fishes are in eastern China, where the anthropogenic SLHs-driven increases in Hg deposition were high (Fig. 1*F*), leading to increases of 9.8% and 9.5% in MeHg exposure from rice and freshwater fishes intake, respectively. Considering production and international trade, seafood consumed in China is mainly from the Northwest Pacific (accounting for 82.6%), where Hg deposition increased most (e.g., by 9.2% in the seafood-producing area of China) as a result of anthropogenic SLHs emissions, resulting in a 7.7% increase in MeHg exposure from seafood intake in China. As one major fishery region in the world, the Northwest Pacific is also the main source of seafood consumed in Japan (65.1%) and South Korea (60.5%), where the MeHg exposure from seafood intake increased by 5.6% and 6.0%, respectively. The national average per-capita seafood consumptions were 43 and 51 kg/y for these two countries, respectively, which were much higher than the global average of 16 kg/y (https://www.fao.org/faostat). As a result, Japan and South Korea experienced a comparable increase in total MeHg exposure to that of China, with increases of 5.8% (9.7 ng $kg^{-1}d^{-1}$) and 6.5% (10.1 ng $kg^{-1}d^{-1}$), respectively. As another large Hg and halogen emitter, the per-capita MeHg exposure in India increased by 7.5% (3.8 ng $kg^{-1}d^{-1}$), with the largest increase from rice intake of 3.0 ng $kg^{-1}d^{-1}$, due to small seafood consumption.

Anthropogenic SLHs-driven changes in MeHg exposure resulted in almost proportional changes of Hg-related health risks. Compared with the NoCont case, the inclusion of anthropogenic SLHs

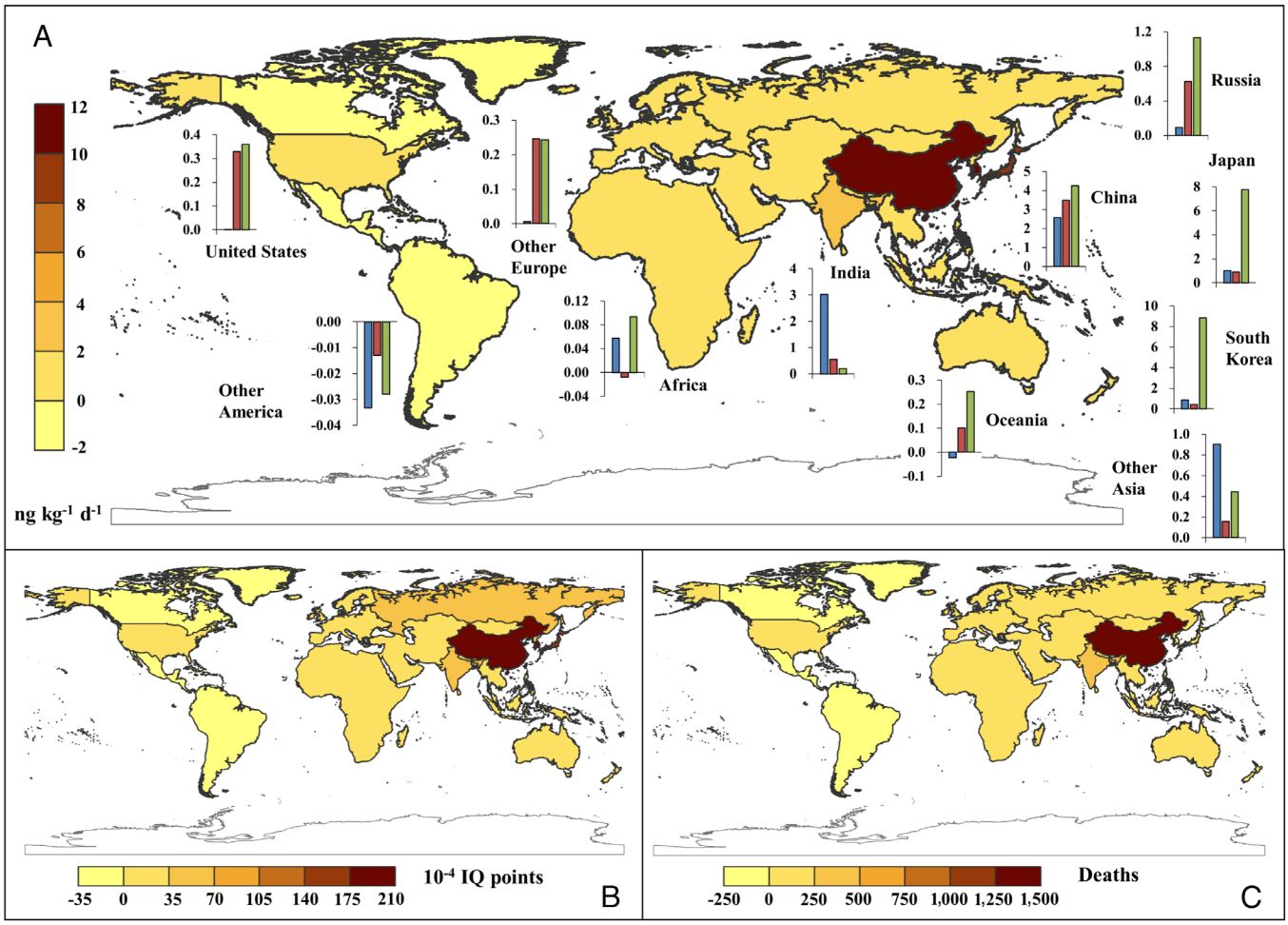

Fig. 2. Global changes in MeHg exposure and related health endpoints driven by anthropogenic SLHs emissions. Anthropogenic SLHs-driven absolute changes in per-capital MeHg exposure (ng kg^{-1} d^{-1}) in 11 continental regions are shown at the *Top* (*A*). The definitions of regions are described in *SI Appendix*, Table S4 and Fig. S8. The total changes are shown in the map, and the individual changes from the intake of rice, freshwater fishes, and seafood are represented by the blue, red, and green bars. Anthropogenic SLHs-driven absolute changes in per-fetus IQ decrements (*B*) and death caused by cardiovascular effects (*C*) are shown at the *Bottom*. Anthropogenic SLHs emissions led to higher MeHg exposure and related health risks in/near regions with high emissions, such as China, India, Japan, and Korea. Decreases occurred in regions with low emissions, such as Other America (America except the United States).

emissions in the HAL case was estimated to increase 0.006 points (0.001 to 0.022 points at a 95% CI; see more details about uncertainty analysis in *SI Appendix*) of per-fetus IQ decrements and 2,169 deaths (496 to 8,632 deaths at a 95% CI) due to cardiovascular effects globally. Asia was the region most affected by MeHg exposure risks driven by anthropogenic SLHs emissions. The anthropogenic SLHs-driven increase in the per-fetus IQ decrements compared with the NoCont case was most significant in China (0.020 points; 0.002 to 0.076 points at a 95% CI), South Korea (0.019 points; 0.001 to 0.088 points at a 95% CI) and Japan (0.017 points; 0.001 to 0.075 points at a 95% CI). In terms of cardiovascular effects, China ranked first, with an increase of 1,361 deaths (271 to 6,071 deaths at a 95% CI), followed by India (358 deaths; 52 to 2,078 deaths at a 95% CI) and Other Asia (161 deaths; 33 to 794 deaths at a 95% CI), compared with the NoCont case. The magnitude of the anthropogenic SLHs-driven increases in Hg-related health risks was related to the increases in MeHg exposure, population, and the baseline incidence of cardiovascular diseases.

Discussion

As a key process governing Hg fate in the atmosphere, Hg oxidation chemistry has been the focus of intense research by the international Hg research community. SLHs are known to play an important role in global Hg oxidation. Observational evidence has demonstrated evidence of anthropogenic SLHs over continental areas. *SI Appendix*, Table S5 lists the recent observations of SLHs over continental regions with anthropogenic origins. However, previous Hg studies considered only the impacts of natural SLHs, i.e., including only natural SLHs emissions but neglecting recently identified anthropogenic SLHs emissions. Here, our results revealed anthropogenic SLHs as a key component of Hg chemical cycling over continental regions, which resulted in increases in continental Hg deposition and human exposure to Hg contamination.

Anthropogenic SLHs and Hg emissions exhibited a similar spatial pattern. Our study showed that the role of such colocated anthropogenic SLHs emissions with Hg in controlling the local Hg^0-$Hg^{I,II}$ conversion and, consequently in regulating Hg deposition, potentially increased human exposure to mercury contamination, especially in the vicinity of SLHs and Hg source regions (Fig. 3). For instance, in China, anthropogenic SLHs emissions led to the increase of surface deposition in polluted regions that can be approximately 20% for total Hg, leading to higher local Hg-related health risks than that previously identified in mercury assessments that did not consider anthropogenic SLHs emissions. Our results provide suggestions and strengthen the incentive for policy makers to implement stricter Hg emission control strategies

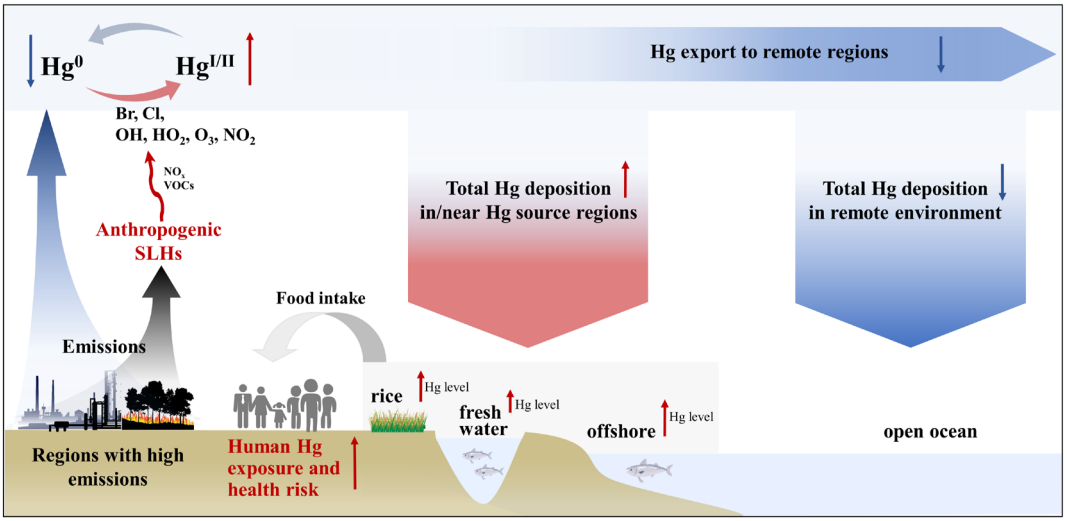

Fig. 3. Conceptual representation of anthropogenic SLHs influence on atmospheric Hg conversion, deposition, and health risks. Colocated anthropogenic SLHs emissions with Hg accelerate Hg^0-$Hg^{I,II}$ conversion through the change in Hg oxidants (Br, Cl, OH, HO_2, O_3, and NO_2), and in turn regulate Hg deposition, with an increase (depicted by red arrows) in Hg deposition over/near Hg source regions and a decrease (depicted by blue arrows) in Hg transport and deposition to remote environments. Larger local Hg deposition can lead to humans in/near Hg source regions suffering from higher Hg exposure from the intake of rice, freshwater fishes, and seafood and consequently higher Hg-related health risks than previous assessments with no consideration of anthropogenic SLHs emissions.

to reduce local Hg-related health risks. In addition, our results imply that anthropogenic SLHs emissions and their impacts should be considered in policies governing Hg emission reductions. For example, Br injection is recommended as an important approach for Hg emission control in the "Guidance on Best Available Techniques and Best Environmental Practices" to fulfill the Minamata Convention on Mercury (32). However, this technology will increase Br emissions to the atmosphere (33), potentially offsetting the effectiveness of Hg emission reduction in decreasing Hg exposure in/near source regions.

In addition to the uncertainties in different steps of our analysis discussed in Supplementary Information, there are additional limitations in this study. For example, this study only included the Hg exposure through food intake from rice, freshwater fishes, and seafood. Other types of food (34) (e.g., eggs, pork, beef) were excluded because of limited available data and much lower MeHg concentrations. We also excluded other minor Hg exposure pathways (35), such as from air inhalation, drinking water, and soil ingestion. Two major health endpoints were selected as a consequence of food Hg exposure, including per-fetus IQ decrements and death caused by cardiovascular effects. Other possible health endpoints (36) were not considered in this study due to the limited data. Therefore, we note that lack of consideration of these other Hg exposure pathways and health endpoints may lead to a potential underestimation of anthropogenic SLHs-driven effects on Hg-related health risk in this study. In addition, our results were based on anthropogenic SLHs emissions in 2014. From 2014 to present-day and in the future, SLHs emissions from coal burning and waste burning are expected to decrease due to stricter emission control although no observational evidence is currently available in this regard. SLHs emissions from biomass burning can be affected by climate change significantly (37, 38). Besides, SLHs emissions from some potential emission sources may increase, such as Br emissions from Br injection technology for Hg emission control (33). Hence, more studies are needed to explore the long-term changes of anthropogenic SLHs emissions and their impacts on Hg-related health risks.

Despite the uncertainties, our results uncover the importance of anthropogenic SLHs emissions on atmospheric Hg fate and health risks over densely populated regions of the world. Therefore, we call for the need to consider anthropogenic SLHs emissions in mercury assessments to improve our knowledge of Hg cycling and its health risks in populated and polluted regions.

Materials and Methods

Emissions of Anthropogenic Inorganic Halogens. Anthropogenic SLHs emissions are not conventionally included in global air pollutant emission inventories, which hinders our assessment of the role of halogen in the atmospheric environment and Hg cycling. We estimated the global emission of reactive inorganic halogen species in 2014, including inorganic chlorine (HCl and fine particle chloride) from coal burning, waste burning and biomass burning, and inorganic bromine (HBr and Br_2) and iodine (HI and I_2) from coal burning. We involved this emission inventory in our previous study to reveal the SLHs effects on climate change (15). Here, we provided more details about the method used to estimate SLHs emissions. The emission factor method was used, following the methodology applied in our previous studies (30, 39). For mainland China, the Cl emission inventory was taken directly from our previous study (39). The detailed local data and county-level activity data compiled in that study were also used to calculate the Br and I emissions in mainland China. Due to limited local data with high resolution, for other regions, country-level coal consumption and solid biofuel consumption were collected from the International Energy Agency (IEA) database (http://www.iea.org). Open burning masses of agricultural residues, forest, grassland, and peat are obtained from the Global Fire Emission Database (GFED4, http://www.globalfiredata.org). Waste burned by open burning was estimated following the method in ref (40). Emission factors of fine particle chloride, and HCl from biomass burning and waste burning were taken from our previous study (39). The emission factors of gas Cl, Br, and I from coal burning were calculated by the following equation:

$$EF_{i,j,k} = C_i R_{j,k} \sum_l \left(1 - f_{(SO_2)i,j,k,l}\eta_{(SO_2)i,j,k,l}\right) \sum_m \left(1 - f_{(PM)i,j,k,m}\eta_{(PM)i,j,k,m}\right), \quad [1]$$

where i, j, k, l, and m represent the halogen species (Cl, Br, and I), sectors, technology types, SO_2 emission control technology, and PM emission control technology, respectively. C is the Cl, Br, or I content in coal (*SI Appendix*, Table S6). The potential impacts of the coal types have not been considered due to the lack of related data. The installation rates of application rates of conventional SO_2 and PM emission control technologies ($f_{(SO2)}$ and $f_{(PM)}$) were from the local database for mainland China (41, 42) and from the PKU-FUEL database (http://inventory.pku.edu.cn/) for other regions. $\eta_{(SO2)}$ and $\eta_{(PM)}$ are the halogen removal efficiencies of these control technologies and R is the halogen release rate, which was obtained from

our previous study (30, 39) for Cl and Br. The I release rates for different combustion technologies and processes are listed in *SI Appendix*, Table S7. The I removal efficiencies (43–45) were set as 5.5% for electrostatic precipitator and fabric filter, 14.5% for wet scrubber, and 90% for flue gas desulfurization. HBr and Br_2, or HI and I_2, were reported to be the two dominant emitted Br or I species from coal burning. Their proportions (46, 47) were set as 70% and 30% for HBr and Br_2, and 95% and 5% for HI and I_2, respectively. *SI Appendix*, Fig. S1 presents the spatial distribution of halogen emissions at a resolution of 1° × 1°. The emission intensity could be greater than 0.2 t $grid^{-1}$ h^{-1} for Cl and 0.01 t $grid^{-1}$ h^{-1} for Br and I in polluted areas. The hot spots of halogen emissions were consistent with those of Hg emissions. The large halogen emitters, China and India, simultaneously contributed nearly half of the global anthropogenic Hg emissions.

CAM-Chem Simulation. We adopted the CAM-Chem (48) coupled with the latest developments of comprehensive SLH sources and chemistry (15) to simulate the spatiotemporal variations in SLHs, along with other key oxidants (OH, HO_2, O_3, etc.) in the atmosphere. The simulations were driven with MERRA2 (Modern-Era Retrospective Analysis for Research and Applications, Version 2) meteorological input data (https://gmao.gsfc.nasa.gov/reanalysis/MERRA-2/). CMIP6 (Coupled Model Intercomparison Project Phase 6) emission data (49, 50) provided anthropogenic emission input for routine air pollutants, e.g., NO, SO_2, CO, NH_3, VOCs, etc., but did not include any reactive halogen species. We performed simulations with a horizontal grid of 1°×1° for 2013 with 1 y as the spin-up. We have conducted two main CAM-Chem simulations, including the NoCont and HAL cases. In the NoCont case, we discarded continental emissions and consider only natural SLHs emissions, mainly from biogenic and photochemical processes in the ocean and polar regions. In the HAL case, we considered natural sources, and anthropogenic SLHs emissions (see *Emission of Anthropogenic Inorganic Halogens* in *Materials and Methods*). The difference between the NoCont and HAL cases was the effect of anthropogenic SLHs emissions.

Our previous studies (15, 17, 18, 51, 52) have shown that the CAM-Chem model provides reasonable estimates of natural halogen species and routine atmospheric composition. Here, we provided further evaluation of simulated SLHs species in continental regions by comparing their abundance with observations reported in the recent past, mainly in China (*SI Appendix*, Fig. S6 and Table S5), including Cl_2, $ClNO_2$, HCl, HOCl, Br_2, BrCl, HOBr, and HBr. The results indicated that our model generally captured the magnitude of and spatial variation in observed Cl species. Br species in highly populated regions were generally underestimated, suggesting that the anthropogenic SLHs-driven effects reported in this study should be considered as a lower limit, especially in polluted regions.

GLEMOS Simulation. We used an updated version of the 3D chemical transport model GLEMOS (Global EMEP Multi-media Modeling System) (53) to quantify the changes in Hg speciation and deposition driven by anthropogenic SLHs emissions. The model simulated emissions, transport, and chemical transformations of Hg species in the atmosphere as well as deposition and air-surface exchange. Six-hourly concentration fields of the chemical reactants Br, Cl, OH, HO_2, O_3, NO_2, HCl, CH_4, and CO participating in Hg chemistry were archived from our CAM-Chem simulations with/without anthropogenic SLHs emissions (HAL and NoCont). Other model configurations were similar to those used in previous studies (8, 54). The model domain had global coverage with a horizontal grid of 3°×3° and included the troposphere and lower stratosphere up to 10 hPa (ca. 30 km). The atmospheric transport of the tracers was driven by meteorological fields generated by the Weather Research and Forecast modeling system (WRF) assimilating the operational analysis data from the European Centre for Medium-Range Weather Forecasts (https://www.ecmwf.int). The updated version of the model simulated Hg^0 and nineteen oxidized $Hg^{I,II}$ species (HgBr, $HgBr_2$, HgBrOH, HgBrCl, HgBrOOH, HgBrONO, HgBrO, HgOH, HgOHOOH, HgOHONO, HgOHO, HgOHOH, HgOHCl, HgCl, $HgCl_2$, HgClO, HgClONO, HgClOOH, and HgO) in both gaseous and particulate forms. Gas–particle partitioning of $Hg^{I,II}$ was parameterized using empirically derived thermodynamic equilibrium mechanism for individual oxidized Hg species following Amos et al. (55) without respeciation in particulate phase. The chemical mechanism included initial Hg^0 oxidation by the radicals Br, Cl, and OH to form unstable Hg^I intermediates, which were further oxidized by these and other reactants (HO_2, O_3, NO_2, HCl, CH_4, CO) to form Hg^{II} or thermally and photoreduced to Hg^0. A detailed description of the reaction kinetics was given in *SI Appendix*, Table S8. Additionally, we incorporated aqueous-phase photoreduction in cloud droplets, using the photolysis rate constant of 0.15 h^{-1} measured in Saiz-Lopez et al. (8) The overall chemical scheme was similar to that applied previously by Shah et al. (12), with the main difference lying in the treatment of the gas–particle interaction of $Hg^{I,II}$ (see more details in S1.2 in *SI Appendix*). We performed simulations for the period 2007 to 2013 using anthropogenic Hg emissions for 2010 (6). Prescribed fluxes of natural and secondary Hg^0 reemissions from soil and seawater were generated depending on the Hg concentration in soil, soil temperature, and solar radiation for emissions from land and proportional to the primary production of organic carbon in seawater for emissions from the ocean (53). Additionally, prompt reemission of Hg from snow was accounted for using an empirical parameterization based on the observational data (56–58). The first 6 y of the period were used for the model spin-up to achieve the steady-state Hg concentrations in the troposphere. The model results were presented as annual averages for 2013.

We evaluated the model performance for elemental Hg, Hg wet deposition, and $Hg^{I,II}$. The overall evaluation primarily relied on comparing observed and simulated Hg^0 concentrations and Hg wet deposition, which were considered the most reliable available Hg observations. While a comparison of model simulations with observations of $Hg^{I,II}$ was included for completeness, it was important to note the well-recognized high uncertainties and the issue of biased low values in the majority of currently available $Hg^{I,II}$ measurement databases (59–62). Detailed statistical analysis of the model evaluation was presented in *SI Appendix*, Text in S2, Tables S9–S11, and Fig. S10. In summary, the model effectively reproduced average measured Hg^0 concentrations (1.63 ng m^{-3}) in both simulation scenarios (1.69 and 1.71 ng m^{-3} for the HAL and NoCont cases, respectively), exhibiting a high spatial correlation coefficient of ~0.88, and a normalized RMSE (NRMSE) of ~23% that slightly decreased when including anthropogenic SLHs emissions. The mean simulated wet deposition (9.59 μg m^{-2} y^{-1} in the HAL case) aligned well with the observed average over all available 134 measurement sites (9.64 μg m^{-2} y^{-1}), with a spatial correlation of 0.52 and a NRMSE of about 50%. The modeled impact of anthropogenic SLHs emissions was most pronounced for urban sites, resulting in an increased correlation from 0.52 to 0.59 and a decreased mean relative bias (MRB) from −5.9% to −3.0%. The model-measurement comparison for $Hg^{I,II}$ concentrations at a limited number of measurement sites revealed a significant overestimation of measured values by the model by more than a factor of 2 (113% in the HAL case), aligning with the acknowledged biased low in the measurements (59–62). The statistical results were significantly influenced by high $Hg^{I,II}$ concentrations measured in the urban environment leading to poor spatial correlation (0.41). However, for rural/remote sites, both correlation (0.88) and overestimation (a factor of 2.5) were considerably more substantial.

Based on the simulation results from GLEMOS, we estimated net atmospheric Hg outflow using the method proposed by Lin et al. (63), as shown below.

$$OF = E - D - NM, \quad [2]$$

where OF, E, D, and NM represent the net atmospheric Hg outflow, Hg emissions, Hg depositions, and net change in mercury mass, respectively.

Changes in Hg Exposure and Health Effects. *SI Appendix*, Fig. S7 illustrates the method used to evaluate the changes in the MeHg exposure and Hg-related health risks caused by anthropogenic SLHs emissions in this study. The intake of rice, freshwater fishes, and seafood was identified as the main route of human Hg exposure, due to the high MeHg concentration and sufficient data sources available for these foods (64). We divided the global continents into 11 regions (i.e., Africa, United States, Other America, China, Japan, South Korea, India, Other Asia, Russia, Other Europe, and Oceania) as our research objects, and divided the global ocean into 19 sea areas based on Food and Agriculture Organization of the United Nations (UN FAO, http://www.fao.org) regional classification method to facilitate the identification of seafood sources (see the definition of regions in *SI Appendix*, Fig. S8 and Table S4). The mercury exposure change for each continental region was calculated as follows:

$$\Delta ME_i = \Sigma_{jk} Per_{ijk} \times I_{ik} \times \Delta C_{jk}, \quad [3]$$

$$Per_{ijk} = \frac{A_{ijk}}{\sum_j A_{ijk}}, \quad [4]$$

where i represents the 11 continental regions; j represents the 11 continental regions and 19 ocean regions; k represents the three food categories; ΔME_i is the changes in human mercury exposure (ng kg^{-1} d^{-1} $capita^{-1}$) in region i resulting from anthropogenic SLHs emissions; Per_{ijk} represents the contribution of region j to the source of consumed food k in region i; A_{ijk} represents the quantity of food k sourced from region j in region i, which is calculated based on the FAO trade dataset (http://www.fao.org); I_{ik} is the food intake for each category (g kg^{-1} d^{-1} $capita^{-1}$) in region i (http://www.fao.org); and ΔC_{jk} represents the concentration change in MeHg (μg kg^{-1}) in food k in source region j.

We compiled the MeHg concentrations in the three foods reported in previous studies and calculate the average in different regions (*SI Appendix*, Tables S1–S3). Then, we used simulated Hg deposition as a proxy to scale the change in MeHg concentration in the three food categories caused by anthropogenic SLHs emissions, following previous studies (34, 65). The freshwater fishes MeHg concentration in source region j was assumed to be proportional to the average total Hg deposition in this region. The seafood and rice MeHg concentrations in source region j were assumed to be proportional to the average total Hg deposition weighted by the spatial distribution of marine fish catch or cropland (66, 67).

The per-fetus IQ decrements and death caused by cardiovascular effects were selected as health endpoints for evaluating changes in mercury exposure (34, 64, 65, 68). We hypothesized a linear dose–response relationship without a threshold between maternal mercury levels (as assessed by hair biomarkers) and newborn IQ decline (34, 64, 65, 68, 69):

$$\Delta IQ = \gamma \lambda \beta \times \Delta ME \times BW, \quad [5]$$

where ΔIQ is the changes in IQ (points) and BW is the average weight of an adult woman. The coefficients β (0.6 μg L^{-1} per μg d^{-1}), λ (0.2 μg g^{-1} per μg L^{-1}), and γ (0.3 IQ points per μg g^{-1}) convert MeHg from intake to blood concentration, blood concentration to hair concentration, and hair concentration to IQ reduction, respectively.

MeHg exposure may also lead to an increased incidence of acute myocardial infarction (AMI). EURAMIC (European Community Multicenter Study of Antioxidants, Myocardial Infarction and Breast Cancer) showed that the dose–response function of MeHg-related AMI was log-linear (70). Therefore, the dose–response relationship was calculated using the following formula (34, 64):

$$\Delta CDA = \sum_g POP_g \times Cf_g \times \omega \times \left(1 - e^{-\phi \lambda \beta \times \Delta ME \times BW}\right), \quad [6]$$

where Δ CDA is the changes in deaths due to AMI, POP_g represents the population of age group g (https://population.un.org), Cf_g represents the crude death rate of all age groups due to cardiovascular diseases (https://www.who.int), ω(0.14) represents the probability of associated causal relationships, reflecting uncertainty based on epidemiological investigations, and ϕ (0.066 per μg g^{-1}) is the correlation coefficient between the concentration of mercury in hair and the risk of heart attack.

Data, Materials, and Software Availability. All study data are included in the article and/or *SI Appendix*. Data related to this article are also available in Zenodo at https://doi.org/10.5281/zenodo.10681794 (71).

ACKNOWLEDGMENTS. This research was supported by Municipal Science and Technology Innovation Commission of Shenzhen (JCYJ20220530143007016), Natural Science Foundation of Guangdong Province (2022A1515010705), National Natural Science Foundation of China (22206106), and Scientific Research Start-up Funds from Tsinghua Shenzhen International Graduate School (QD2021015C). The team of Spanish National Research Council is supported by the European Research Council Executive Agency under the European Union's Horizon 2020 Research and Innovation Programme (Project ERC-2016-COG 726349 CLIMAHAL, awarded to A.S.-L.). Contribution of Oleg Travnikov wasfunded by the Global Mercury Observation System (GMOS)-Train project of the European Union's Horizon 2020 research and innovation programme under the Marie Sklodowska-Curie grant agreement no. 860497 and cofunded by the Slovenian Research Agency Research Programme P1-0143 and J1-3033 (IsoCont). Contribution of Shuxiao Wang is supported by the National Natural Science Foundation of China (Project 92044302). The HKPolyU team is supported by the Hong Kong Research Grants Council (Project T24-504/17-N, awarded to T.W.). A.S.M. is supported by the Ministry of Earth Sciences, Government of India.

Author affiliations: [a]Institute of Environment and Ecology, Tsinghua Shenzhen International Graduate School, Tsinghua University, Shenzhen 518055, China; [b]Department of Environmental Sciences, Jožef Stefan Institute, Ljubljana 1000, Slovenia; [c]Department of Atmospheric Chemistry and Climate, Institute of Physical Chemistry Blas Cabrera, Spanish National Research Council, Madrid 28006, Spain; [d]Department of Civil and Environmental Engineering, The Hong Kong Polytechnic University, Hong Kong 999077, China; [e]Environment Research Institute, Shandong University, Qingdao 266237, China; [f]Institute for Interdisciplinary Science, National Research Council, School of Natural Sciences, National University of Cuyo, Mendoza M5502JMA, Argentina; [g]Centre for Climate Change Research, Indian Institute of Tropical Meteorology, Ministry of Earth Sciences, Pashan, Pune 411008, India; and [h]State Key Joint Laboratory of Environmental Simulation and Pollution Control, School of Environment, Tsinghua University, Beijing 100084, China

Author contributions: X.F. and A.S.-L. designed research; X.F., X.S., O.T., Q.L., and A.S.-L. performed research; X.F., X.S., O.T., Q.L., and A.S.-L. contributed new reagents/analytic tools; X.F., X.S., O.T., Q.L., C.Q., C.A.C., R.P.F., A.S.M., S.W., T.W., and A.S.-L. analyzed data; and X.F., X.S., O.T., Q.L., and A.S.-L. wrote the paper.

1. C. T. Driscoll, R. P. Mason, H. M. Chan, D. J. Jacob, N. Pirrone, Mercury as a global pollutant: Sources, pathways, and effects. *Environ. Sci. Technol.* **47**, 4967–4983 (2013).
2. F. Beckers, J. Rinklebe, Cycling of mercury in the environment: Sources, fate, and human health implications: A review. *Crit. Rev. Environ. Sci. Technol.* **47**, 693–794 (2017).
3. P. Grandjean, H. Satoh, K. Murata, K. Eto, Adverse effects of methyl-mercury: Environmental health research implications. *Environ. Health Perspect.* **118**, 1137–1145 (2010).
4. H. A. Roman *et al.*, Evaluation of the cardiovascular effects of methylmercury exposures: Current evidence supports development of a dose–response function for regulatory benefits analysis. *Environ. Health Perspect.* **119**, 607–614 (2011).
5. D. G. Streets *et al.*, Total mercury released to the environment by human activities. *Environ. Sci. Technol.* **51**, 5969–5977 (2017).
6. AMAP/UN Environment, *Technical Background Report for the Global Mercury Assessment 2018* (Arctic Monitoring and Assessment Programme/UN Environment Programme, Chemicals and Health Branch, Oslo, Norway/Geneva, Switzerland, 2019), viii, 426pp, including E-Annexes.
7. P. A. Ariya *et al.*, Mercury physicochemical and biogeochemical transformation in the atmosphere and at atmospheric interfaces: A review and future directions. *Chem. Rev.* **115**, 3760–3802 (2015).
8. A. Saiz-Lopez *et al.*, Photoreduction of gaseous oxidized mercury changes global atmospheric mercury speciation, transport and deposition. *Nat. Commun.* **9**, 4796 (2018).
9. C. D. Holmes, D. J. Jacob, X. Yang, Global lifetime of elemental mercury against oxidation by atomic bromine in the free troposphere. *Geophys. Res. Lett.* **33**, L20808 (2006).
10. H. M. Horowitz *et al.*, A new mechanism for atmospheric mercury redox chemistry: Implications for the global mercury budget. *Atmos. Chem. Phys.* **17**, 6353–6371 (2017).
11. F. Wang *et al.*, Enhanced production of oxidised mercury over the tropical Pacific Ocean: A key missing oxidation pathway. *Atmos. Chem. Phys.* **14**, 1323–1335 (2014).
12. V. Shah *et al.*, Improved mechanistic model of the atmospheric redox chemistry of mercury. *Environ. Sci. Technol.* **55**, 14445–14456 (2021).
13. A. Saiz-Lopez, R. von Glasow, Reactive halogen chemistry in the troposphere. *Chem. Soc. Rev.* **41**, 6448–6472 (2012).
14. W. R. Simpson, S. S. Brown, A. Saiz-Lopez, J. A. Thornton, R. von Glasow, Tropospheric halogen chemistry: Sources, cycling, and impacts. *Chem. Rev.* **115**, 4035–4062 (2015).
15. A. Saiz-Lopez *et al.*, Natural short-lived halogens exert an indirect cooling effect on climate. *Nature* **618**, 967–973 (2023).
16. L. J. Carpenter *et al.*, Atmospheric iodine levels influenced by sea surface emissions of inorganic iodine. *Nat. Geosci.* **6**, 108–111 (2013).
17. F. Iglesias-Suarez *et al.*, Natural halogens buffer tropospheric ozone in a changing climate. *Nat. Clim. Change* **10**, 147 (2020).
18. C. Ordonez *et al.*, Bromine and iodine chemistry in a global chemistry-climate model: Description and evaluation of very short-lived oceanic sources. *Atmos. Chem. Phys.* **12**, 1423–1447 (2012).
19. L. Zhu *et al.*, Effect of sea salt aerosol on tropospheric bromine chemistry. *Atmos. Chem. Phys.* **19**, 6497–6507 (2019).
20. D. Obrist *et al.*, Bromine-induced oxidation of mercury in the mid-latitude atmosphere. *Nat. Geosci.* **4**, 22–26 (2011).
21. W. H. Schroeder *et al.*, Arctic springtime depletion of mercury. *Nature* **394**, 331–332 (1998).
22. S. Wang *et al.*, Direct detection of atmospheric atomic bromine leading to mercury and ozone depletion. *Proc. Natl. Acad. Sci. U.S.A.* **116**, 14479–14484 (2019).
23. C. D. Holmes *et al.*, Global atmospheric model for mercury including oxidation by bromine atoms. *Atmos. Chem. Phys.* **10**, 12037–12057 (2010).
24. J. P. Parrella *et al.*, Tropospheric bromine chemistry: Implications for present and pre-industrial ozone and mercury. *Atmos. Chem. Phys.* **12**, 6723–6740 (2012).
25. S. S. Gunthe *et al.*, Enhanced aerosol particle growth sustained by high continental chlorine emission in India. *Nat. Geosci.* **14**, 77–84 (2021).
26. X. Peng *et al.*, Photodissociation of particulate nitrate as a source of daytime tropospheric Cl-2. *Nat. Commun.* **13**, 939 (2022).
27. X. Peng *et al.*, An unexpected large continental source of reactive bromine and chlorine with significant impact on wintertime air quality. *Natl. Sci. Rev.* **8**, nwaa304 (2021).
28. M. Xia *et al.*, Pollution-derived Br2 boosts oxidation power of the coastal atmosphere. *Environ. Sci. Technol.* **56**, 12055–12065 (2022).

29. Q. Li *et al.*, Potential effect of halogens on atmospheric oxidation and air quality in China. *J. Geophys. Res. Atmos.* **125**, e2019JD032058 (2020).
30. Q. Li *et al.*, Halogens enhance haze pollution in China. *Environ. Sci. Technol.* **55**, 13625–13637 (2021).
31. X. Wang *et al.*, Effects of anthropogenic chlorine on PM2.5 and ozone air quality in China. *Environ. Sci. Technol.* **54**, 9908–9916 (2020).
32. United Nations Envieonment Programme (UNEP), *Guidance on Best Available Techniques and Best Environmental Practices Taking into Account any Difference between New and Existing Sources and the Need to Minimize Cross-Media Effects* (Geneva, Switzerland, 2017).
33. Q. Wu *et al.*, Enhanced mercury control but increased bromine and sulfur trioxides emissions after using bromine injection technology based on full-scale experiment. *Fuel* **285**, 119130 (2021).
34. L. Chen *et al.*, Trans-provincial health impacts of atmospheric mercury emissions in China. *Nat. Commun.* **10**, 1484 (2019).
35. B.-J. Ye *et al.*, Evaluation of mercury exposure level, clinical diagnosis and treatment for mercury intoxication. *Ann. Occup. Environ. Med.* **28**, 5 (2016).
36. M. R. Karagas *et al.*, Evidence on the human health effects of low-level methylmercury exposure. *Environ. Health Perspect.* **120**, 799–806 (2012).
37. C. D. Bray, W. H. Battye, V. P. Aneja, W. H. Schlesinger, Global emissions of NH_3, NOx, and N_2O from biomass burning and the impact of climate change. *J. Air Waste Manage. Assoc.* **71**, 102–114 (2021).
38. R. O. Corona-Nunez, J. E. Campo, Climate and socioeconomic drivers of biomass burning and carbon emissions from fires in tropical dry forests: A Pantropical analysis. *Global Change Biol.* **29**, 1062–1079 (2022).
39. X. Fu *et al.*, Anthropogenic emissions of hydrogen chloride and fine particulate chloride in China. *Environ. Sci. Technol.* **52**, 1644–1654 (2018).
40. C. Wiedinmyer, R. J. Yokelson, B. K. Gullett, Global emissions of trace gases, particulate matter, and hazardous air pollutants from open burning of domestic waste. *Environ. Sci. Technol.* **48**, 9523–9530 (2014).
41. Q. Ma *et al.*, Impacts of coal burning on ambient PM2.5 pollution in China. *Atmos. Chem. Phys.* **17**, 4477–4491 (2017).
42. S. X. Wang *et al.*, Emission trends and mitigation options for air pollutants in East Asia. *Atmos. Chem. Phys.* **14**, 6571–6603 (2014).
43. M. Bettinelli, S. Spezia, C. Minoia, A. Ronchi, Determination of chlorine, fluorine, bromine, and iodine in coals with ICP-MS and IC. *At. Spectrosc.* **23**, 105–110 (2002).
44. D. Wu *et al.*, Estimation of atmospheric iodine emission from coal combustion. *Int. J. Environ. Sci. Technol.* **11**, 357–366 (2014).
45. R. Meij, H. te Winkel, The emissions of heavy metals and persistent organic pollutants from modern coal-fired power stations. *Atmos. Environ.* **41**, 9262–9272 (2007).
46. P. Bing-Xian, L. Lan, W. Dai-She, Distribution of bromine and iodine in thermal power plant. *J. Coal Sci. Eng. (China)* **19**, 387–391 (2013).
47. Y.-Q. Jin, L. Tao, Y. Chi, J.-H. Yan, Conversion of bromine during thermal decomposition of printed circuit boards at high temperature. *J. Hazard. Mater.* **186**, 707–712 (2011).
48. J. F. Lamarque *et al.*, CAM-chem: Description and evaluation of interactive atmospheric chemistry in the Community Earth System Model. *Geosci. Model Dev.* **5**, 369–411 (2012).
49. M. J. Gidden *et al.*, Global emissions pathways under different socioeconomic scenarios for use in CMIP6: A dataset of harmonized emissions trajectories through the end of the century. *Geosci. Model Dev.* **12**, 1443–1475 (2019).
50. R. M. Hoesly *et al.*, Historical (1750–2014) anthropogenic emissions of reactive gases and aerosols from the Community Emissions Data System (CEDS). *Geosci. Model Dev.* **11**, 369–408 (2018).
51. Q. Li *et al.*, Reactive halogens increase the global methane lifetime and radiative forcing in the 21st century. *Nat. Commun.* **13**, 2768 (2022).
52. A. Saiz-Lopez *et al.*, Iodine chemistry in the troposphere and its effect on ozone. *Atmos. Chem. Phys.* **14**, 13119–13143 (2014).
53. O. Travnikov *et al.*, Multi-model study of mercury dispersion in the atmosphere: Atmospheric processes and model evaluation. *Atmos. Chem. Phys.* **17**, 5271–5295 (2017).
54. A. Saiz-Lopez *et al.*, Photochemistry of oxidized Hg(I) and Hg(II) species suggests missing mercury oxidation in the troposphere. *Proc. Natl. Acad. Sci. U.S.A.* **117**, 30949–30956 (2020).
55. H. M. Amos *et al.*, Gas-particle partitioning of atmospheric Hg(II) and its effect on global mercury deposition. *Atmos. Chem. Phys.* **12**, 591–603 (2012).
56. K. P. Johnson, J. D. Blum, G. J. Keeler, T. A. Douglas, Investigation of the deposition and emission of mercury in arctic snow during an atmospheric mercury depletion event. *J. Geophys. Res. Atmos.* **113**, D17304 (2008).
57. J. L. Kirk, V. L. S. Louis, M. J. Sharp, Rapid reduction and reemission of mercury deposited into snowpacks during atmospheric mercury depletion events at Churchill, Manitoba, Canada. *Environ. Sci. Technol.* **40**, 7590–7596 (2006).
58. F. Sprovieri, N. Pirrone, M. S. Landis, R. K. Stevens, Atmospheric mercury behavior at different altitudes at Ny Alesund during Spring 2003. *Atmos. Environ.* **39**, 7646–7656 (2005).
59. S. M. Dunham-Cheatham, S. Lyman, M. S. Gustin, Comparison and calibration of methods for ambient reactive mercury quantification. *Sci. Total Environ.* **856**, 159219 (2023).
60. M. S. Gustin *et al.*, Use of membranes and detailed HYSPLIT analyses to understand atmospheric particulate, gaseous oxidized, and reactive mercury chemistry. *Environ. Sci. Technol.* **55**, 893–901 (2021).
61. M. S. Gustin *et al.*, Do we understand what the mercury speciation instruments are actually measuring? Results of RAMIX. *Environ. Sci. Technol.* **47**, 7295–7306 (2013).
62. N. Marusczak, J. E. Sonke, X. Fu, M. Jiskra, Tropospheric GOM at the Pic du Midi Observatory–Correcting bias in Denuder based observations. *Environ. Sci. Technol.* **51**, 863–869 (2017).
63. C. J. Lin *et al.*, Estimating mercury emission outflow from East Asia using CMAQ-Hg. *Atmos. Chem. Phys.* **10**, 1853–1864 (2010).
64. Y. Zhang *et al.*, Global health effects of future atmospheric mercury emissions. *Nat. Commun.* **12**, 3035 (2021).
65. A. Giang, N. E. Selin, Benefits of mercury controls for the United States. *Proc. Natl. Acad. Sci. U.S.A.* **113**, 286–291 (2016).
66. D. Grogan, S. Frolking, D. Wisser, A. Prusevich, S. Glidden, Global gridded crop harvested area, production, yield, and monthly physical area data circa 2015. *Sci. Data* **9**, 15 (2022).
67. R. A. Watson, A database of global marine commercial, small-scale, illegal and unreported fisheries catch 1950–2014. *Sci. Data* **4**, 170039 (2017).
68. G. E. Rice, J. K. Hammitt, J. S. Evans, A probabilistic characterization of the health benefits of reducing methyl mercury intake in the United States. *Environ. Sci. Technol.* **44**, 5216–5224 (2010).
69. D. A. Axelrad, D. C. Bellinger, L. M. Ryan, T. J. Woodruff, Dose–response relationship of prenatal mercury exposure and IQ: An integrative analysis of epidemiologic data. *Environ. Health Perspect.* **115**, 609–615 (2007).
70. K. Landmark, I. Aursnes, Mercury, fish, fish oil and the risk of cardiovascular disease. *Tidsskr. Nor. Laegeforen.* **124**, 198–200 (2004).
71. X. Fu *et al.*, Dataset for Anthropogenic short-lived halogens increase human exposure to mercury contamination due to enhanced mercury oxidation [Data set]. Zenodo. https://doi.org/10.5281/zenodo.10681794. Deposited 20 February 2024.